scientific reports

Check for updates

OPEN

Integrable quantum many-body sensors for AC field sensing

Utkarsh Mishra✉ & Abolfazl Bayat✉

Quantum sensing is inevitably an elegant example of the supremacy of quantum technologies over their classical counterparts. One of the desired endeavors of quantum metrology is AC field sensing. Here, by means of analytical and numerical analysis, we show that integrable many-body systems can be exploited efficiently for detecting the amplitude of an AC field. Unlike the conventional strategies in using the ground states in critical many-body probes for parameter estimation, we only consider partial access to a subsystem. Due to the periodicity of the dynamics, any local block of the system saturates to a steady state which allows achieving sensing precision well beyond the classical limit, almost reaching the Heisenberg bound. We associate the enhanced quantum precision to closing of the Floquet gap, resembling the features of quantum sensing in the ground state of critical systems. We show that the proposed protocol can also be realized in near-term quantum simulators, e.g. ion-traps, with a limited number of qubits. We show that in such systems a simple block magnetization measurement and a Bayesian inference estimator can achieve very high precision AC field sensing.

Quantum systems have emerged as excellent sensors for detecting various types of fields[1], including weak magnetic[2–7], electric[8–12], and gravitational fields[13], due to their extreme sensitivity against variation in the environment. The prospect of applications for quantum sensing is very wide covering material science[14] to biomedical analysis[15,16]. In particular, AC field sensing has been the subject of intense theoretical and experimental research for the estimation of amplitude[17–19], frequency[20,21], and phase[22–28]. The majority of these protocols, mainly implemented in nitrogen vacancy centers, utilize a series of spin-echo pulses to accumulate the information about the AC field in the phase of a coherent superposition of a single qubit, which is then converted into the amplitude at the readout stage[29–31]. However, the ultimate precision is limited by the number of spin-echo pulses that one can apply within the coherence time. To enhance the precision, one can increase the number of particles, although, once the particles start to interact, the precision is severely hindered[32]. In Ref.[33], a complex pulse structure has been designed to suppress the interaction between the particles and enhance the sensing precision. Therefore, an important open question is whether one can go beyond the spin-echo procedure and harness the interaction between particles, instead of suppressing it, for AC field sensing.

The quality of any sensing protocol, either classical or quantum, is quantified by the uncertainty in the estimation of an unknown parameter h which is fundamentally bounded by the Cramér–Rao inequality as $\mathrm{Var}\,(h) \geq 1/F$[34]. Here, $\mathrm{Var}\,(h)$ is the variance of the estimation with respect to an unbiased estimator, $F \sim L^{\eta}$ is the Fisher information, L is the number of resources, and η is a positive constant (See Refs.[35,36] for a recent review on quantum Fisher information). Classical systems, at best, can result in $\eta = 1$ known as the standard limit. By harnessing quantum entanglement, e.g. in the specific form of GHZ[37] and N00N[38] states, one can enhance the sensitivity to $\eta = 2$, known as the Heisenberg limit. However, these states are extremely sensitive to decoherence and particle loss[39,40] making them impractical for real applications. In addition, any interaction between the particles deteriorates the sensing quality[41]. One can also exceed the standard limit through adaptive[42–48] or continuous measurements[49] using single particle sensors.

While in the GHZ-based quantum sensing, the interaction between particles should be avoided, in a fundamentally different route, one can harness the interaction in strongly correlated many-body quantum systems in[50–56] and out[57–62] of equilibrium for sensing. In fact, thanks to the emergent of multipartite entanglement[63–68], many-body systems near criticality provide enhanced quantum precision of $\eta = 2/\nu$[50–55], where ν is the critical exponent in charge of the divergence of correlation length[69,70]. In addition, the evolution of many-body systems has also been used for sensing local[62] and global[71] DC fields as well as extracting information about the spectral structure of time-varying fields[72–74]. In most of these works, either static or dynamic, it is dominantly assumed that the whole system is accessible for measurement which may not be practical. Nonetheless, quantum enhancement in many-body sensors with only partial access to a subsystem has hardly been explored and it is not clear whether criticality can still enhance the precision in such scenarios. One may raise question whether strongly

Institute of Fundamental and Frontier Sciences, University of Electronic Science and Technology of China, Chengdu 610051, China. ✉email: utkarsh.mishra@uestc.edu.cn; abolfazl.bayat@uestc.edu.cn

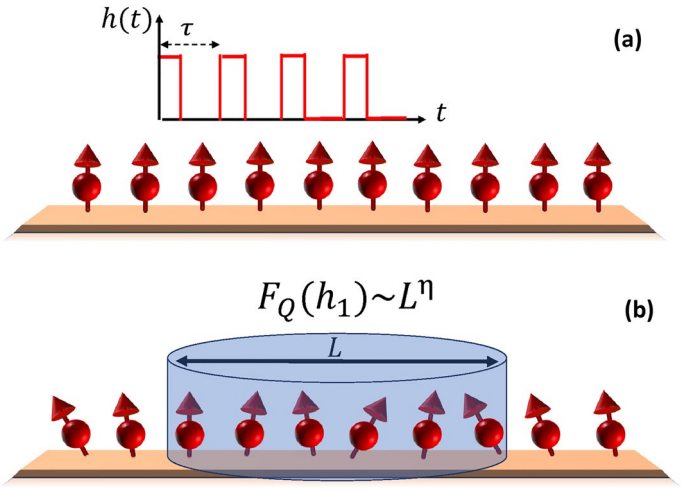

Figure 1. (**a**) The many-body quantum system of spin-1/2 particles, prepared in its ground state, is interacting with a time-periodic magnetic field, $h(t)$, of period τ and strength h_1. (**b**) In the steady state, a block of L contiguous spins are measured resulting in a quantum Fisher information which scales with L as $F_Q(h_1) \sim L^{\eta}$.

correlated many-body systems can also be beneficial for AC field sensing. If so, do they provide precision beyond the standard limit? What would happen if only partial access to a subsystem is available? The importance lies in the fact that the AC field excites high energy eigenstates and thus the notion of ground state criticality will no longer exist and thus a new theory is needed. Recently, we have shown that one can gain quantum enhanced sensing in periodically driven systems even with the partial accessibility for sensing DC magnetic fields[75]. Here, we generalize this approach for sensing AC magnetic fields. In the present work, we also demonstrate the practicality of the sensing protocol using Bayesian inference.

The main findings of the paper are: (i) the quantum Fisher information of a block, with respect to amplitude of the AC magnetic field, peaks along a line, making it far more versatile than the critical systems; (ii) the line of the peak of the quantum Fisher information coincides with the line of vanishing Floquet gap; and (iii) at the closing of the Floquet gap, the quantum Fisher information scales well beyond the standard limit, shows quantum enhanced sensing. Finally, we numerically analyze the proposal for an ion trap.

Results

The setup for sensing. We consider an interacting spin-1/2 Ising chain of length N in a transverse field to serve as a many-body probe for sensing a time-periodic magnetic field, $h(t)$, which is assumed to be along the transverse direction. The Hamiltonian of the model is written as

$$H(t) = -J\sum_{i=1}^{N}\hat{\sigma}_i^x\hat{\sigma}_{i+1}^x - \sum_i (h_0 + h(t))\hat{\sigma}_i^z, \tag{1}$$

where, $J > 0$ is the nearest-neighbor spin-spin interaction, h_0 is a DC external magnetic field which is tunable, $\hat{\sigma}_i^{x/z}$ are Pauli matrices at site i, and the periodic boundary conditions is assumed, i.e., $\hat{\sigma}_{N+1}^{x/z} = \hat{\sigma}_1^{x/z}$. In the absence of $h(t)$, the Hamiltonian in Eq. (1) is known to exhibit a quantum phase transition at $h_0 = h_c$ such that $h_c/J = 1$. The time-dependent field $h(t)$, as we will show later, can be any periodic function with a nonzero mean over a period, such as Dirac delta-kick or square pulses. A schematic picture of the system is given in Fig. 1. To begin with, the time-dependent form of the magnetic field, $h(t)$, is taken in the form of a Dirac delta-kick as

$$h(t) = h_1\sum_{n=0}^{n=\infty}\delta(t - n\tau), \tag{2}$$

where, the strength of the kick is h_1 whose estimation will be investigated in this paper. The above Hamiltonian in the presence of $h(t)$, Eq. (2), is time periodic, i.e., $H(t) = H(t + n\tau)$ with τ being the time period, which is known a priory, and n being integer valued. The time evolution monitored in steps of $t = n\tau$ is referred as *stroboscopic* in the literature[76,77]. The initial state of the evolution is taken to be a fully polarized state where each spins are in the eigenbasis of $\hat{\sigma}_z$ with eigenvalue $+1$, i.e., $|\Psi(0)\rangle = |\uparrow\otimes\uparrow\otimes\cdots\otimes\uparrow\rangle$. The role of other initial states is discussed in more detail later. The time evolved state of the system is $|\Psi(t)\rangle = U(t,0)|\Psi(0)\rangle$, where

$$U(t,0) = \mathscr{T}\, e^{-i\int_0^t H(t)dt}, \tag{3}$$

with $\mathscr{T}$ being the time order operator. For such a case, the subsequent dynamics can be obtained from the knowledge of one time period propagator $U(\tau,0)$ and is termed as Floquet operator. The Floquet evolution has already been found useful in explaining the emergence of thermal states under periodic driving[77], engineering exotic

topological phases of matter[78], dynamically decoupling the interaction between the particles[20,33] and efficiently being simulated on digital quantum simulators[79].

The Hamiltonian in Eq. (1) can be solved exactly using Jordan-Wigner transformation (JW), as elaborated in[80,81]. We outline the key steps and present detailed calculations in the Supplementary Materials (SM) S1. The first step is to map the spin operators, $\hat{\sigma}_i$, into fermionic operators, $\hat{c}_i^\dagger(\hat{c}_i)$, via the JW transformations:

$$\begin{aligned}\hat{\sigma}_j^- &= e^{i\pi\sum_{i=1}^{j-1}\hat{\sigma}_i^+\hat{\sigma}_i^-}c_j\\ \hat{\sigma}_j^+ &= c_j^\dagger e^{-i\pi\sum_{i=1}^{j-1}\hat{\sigma}_i^+\hat{\sigma}_i^-},\end{aligned} \tag{4}$$

where, $\hat{\sigma}_j^\pm = (\hat{\sigma}_j^x \pm \hat{\sigma}_j^y)/2$. By defining Fourier space fermionic operator as $d_k = \frac{1}{\sqrt{N}}\sum_j e^{ikj}c_j$, one gets $H(t) = \sum_k H_k$, where H_k being the Hamiltonian of the kth subspace given by $H_k = (h(t) + J\cos(k))(d_k^\dagger d_k - d_{-k}d_{-k}^\dagger) + J\sin(k)(d^\dagger d_{-k}^\dagger - d_k d_{-k})$. The time-evolved state can be obtained using Eq. (3) and the fact that the Hamiltonian is a sum of independent modes, k, as

$$\begin{aligned}|\Psi(t=n\tau)\rangle &= [U(\tau,0)]^n|\Psi(0)\rangle = e^{-inH^F\tau}|\Psi(0)\rangle\\ &= \otimes_{k>0}\, e^{-inH_k^F\tau}|\psi_k^0\rangle.\end{aligned} \tag{5}$$

Here, $|\Psi(0)\rangle = \otimes_k|\psi_k^0\rangle$ is the initial state and H_k^F is termed as Floquet Hamiltonian. The Floquet Hamiltonian H_k^F turns out to be simple to obtain for the delta-kick field. If, over a period τ, the initial and the final Hamiltonians are H_k^i and H_k^f, respectively, then

$$H_k^F = |\vec{\mu}_k^F|\hat{n}_k^F.\vec{\sigma}_p, \tag{6}$$

where, $\vec{\sigma}_p = (\hat{\sigma}_p^x, \hat{\sigma}_p^y, \hat{\sigma}_p^z)$ are the pseudospin-1/2 operators, $\hat{n}_k^F = \vec{\mu}_k^F/|\vec{\mu}_k^F|$, and the Floquet quasi energies $|\vec{\mu}_k^F|$ are given by

$$\begin{aligned}|\vec{\mu}_k^F| = \frac{1}{\tau}\cos^{-1}\Big[&\cos(|\vec{\mu}_k^i|\tau)\cos(|\vec{\mu}_k^f|\tau)\\ &- \hat{n}_k^i\cdot\hat{n}_k^f\sin(|\vec{\mu}_k^i|\tau)\sin(|\vec{\mu}_k^f|\tau)\Big],\end{aligned} \tag{7}$$

and

$$\begin{aligned}\hat{n}_k^F = \frac{1}{\sin(|\vec{\mu}_k^F|\tau)}\Big[&\hat{n}_k^i\sin(|\vec{\mu}_k^i|\tau)\cos(|\vec{\mu}_k^f|\tau)\\ &+ \hat{n}_k^f\sin(|\vec{\mu}_k^f|\tau)\cos(|\vec{\mu}_k^i|\tau)\\ &- \hat{n}_k^i\times\hat{n}_k^f\sin(|\vec{\mu}_k^i|\tau)\sin(|\vec{\mu}_k^f|\tau)\Big],\end{aligned} \tag{8}$$

where, $H_k^i = |\vec{\mu}_k^i|\hat{n}_k^i.\vec{\sigma}_p$ and similarly for H_k^f with $\hat{n}_k^{i(f)} = \vec{\mu}_k^{i(f)}/|\vec{\mu}_k^{i(f)}|$. For the delta-kick magnetic field, $\vec{\mu}_k^i = (0, J\sin(k), h_0 + J\cos(k))$, $\vec{\mu}_k^f = (0,0,h_1)$, and the Floquet Hamiltonian, obtained in Eq. (6), is a 2×2 matrix.

For a given wave function $|\Psi(t)\rangle$ of a many-body quantum system, partial accessibility on a length scale $L \ll N$ is well described by a reduced density matrix, ρ_L, which is given by

$$\rho_L(t) = \mathrm{Tr}_{N-L}|\Psi(t)\rangle\langle\Psi(t)|, \tag{9}$$

where Tr_{N-L} stands for the partial trace overall sites except the spins within the block L. It is worth emphasizing that although the density matrix of the full system, given by $\rho(t) = |\Psi(t)\rangle\langle\Psi(t)|$, is pure, the density matrix $\rho_L(t)$ is mixed as the state $|\Psi(t)\rangle$ gets more entangled with increasing t. Thanks to the periodic boundary condition, the choice of the location of the block is irrelevant and only its size L is important. As the system evolves, the information of h_1 is imprinted on the quantum state $\rho_L(t)$ which can be extracted by performing proper measurements and feeding the results into an estimator algorithm, such as Bayesian inference (the details are presented in Sec. "Effect of the total system size"). In the long-time, as we will see in the following sections, the dynamics of the observables associated with ρ_L equilibrate to a steady state value, which will be incorporated into our sensing protocol for estimating h_1. One can properly tune the DC field h_0, as an extra controllable parameter, to enhance the sensitivity of the system to the variation of h_1. Moreover, without loss of generality, we fix the time-period τ to be $J\tau = 0.2$ as, we will see that, for all $J\tau \leq 1$ the local steady state can be used for parameter estimation.

Estimation theory. We, in this section, review the quantum estimation theory for inferring an unknown parameter encoded in a general density matrix. Any estimation protocol relies on two crucial ingredients: (i) a measurement setup that measures the system on a specific basis and (ii) an estimator algorithm that uses the measured data for inferring the value of the unknown parameter. The precision of estimating the unknown parameter, h_1, quantified by the statistical variance, is bounded by the Cramér–Rao inequalities[28,34]

$$\mathrm{Var}\,(h_1) \geq \frac{1}{MF_C(h_1)} \geq \frac{1}{MF_Q(h_1)}, \tag{10}$$

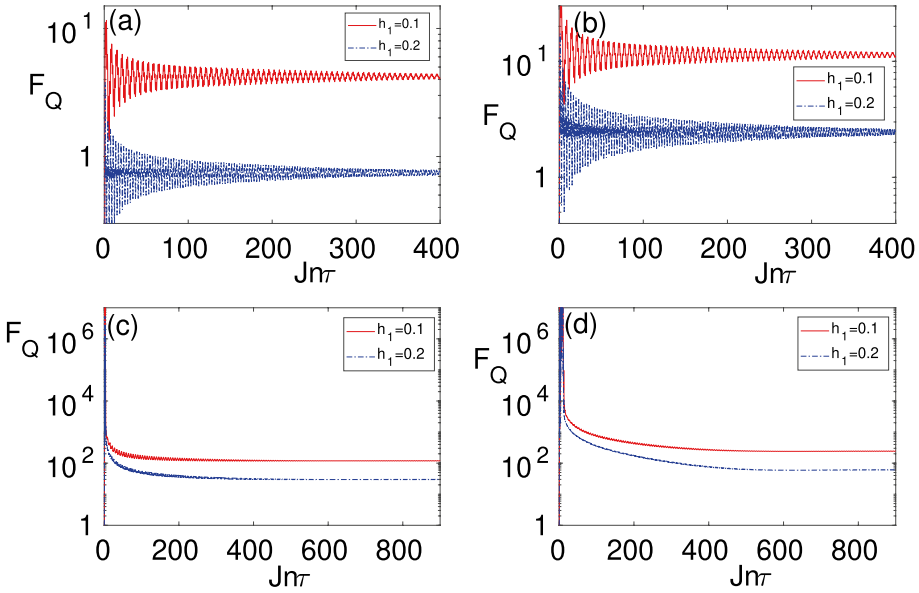

Figure 2. The time-evolution of quantum Fisher information F_Q as a function of time $t = n\tau$ for different values of $h_1/J = 0.1$ (regular red line), $h_1/J = 0.2$ (dashed dotted blue line) and various block sizes: (**a**) $L = 1$; (**b**) $L = 2$; (**c**) $L = 10$; and (**d**) $L = 20$.

where, M is the number of samples, F_C and F_Q are the classical and quantum Fisher information, respectively. The above inequalities show that the variance of any *unbiased* estimator of a parameter cannot be lower than the inverse of the Fisher information. When the measurement basis is fixed, say by a set of positive valued measurements (POVM) $\{\Pi_r\}$, the above inequality is bounded by the classical Fisher Information (CFI) F_C, which is also known as the classical Cramér–Rao inequality. In this case, the equality is achieved when the estimator algorithm is optimized. The classical Fisher information is given by

$$F_C(h_1) = \sum_r \frac{(\partial_{h_1} p_r)^2}{p_r}, \tag{11}$$

where, $p_r(h_1) = \text{Tr}\,[\rho_L(h_1)\Pi_r]$ is the probability of obtaining the outcome r and $\partial_{h_1} p_r = \frac{\partial p_r}{\partial h_1}$. Since the POVM satisfies $\sum_r \Pi_r^\dagger \Pi_r = \mathbb{I}$, where $\mathbb{I}$ is the identity matrix in the state space, it automatically implies that $\sum_r p_r = 1$. One can further tighten the classical Cramér–Rao inequality by optimizing the measurement basis over all possible POVMs which then results in a new bound, given by the quantum Fisher information (QFI) F_Q, as stated in Eq. (10). In this case, the inequality is called the quantum Cramér–Rao inequality. Note that the QFI is independent of the measurement basis and the equality is achieved when both estimation algorithm and measurement basis are chosen to be optimal.

For the density matrix, ρ_L, the QFI is given by[28]

$$F_Q = \sum_{r,s=1}^{2L} \frac{2\Re(\langle\lambda_r|\partial_{h_1}\rho_L|\lambda_s\rangle\langle\lambda_s|\partial_{h_1}\rho_L|\lambda_r\rangle)}{\lambda_r + \lambda_s}, \tag{12}$$

where, $\rho_L = \sum_{r=1}^{2L} \lambda_r |\lambda_r\rangle\langle\lambda_r|$ is the spectral decomposition of ρ_L with λ_r and $|\lambda_r\rangle$ being the eigenvalues and eigenvectors, respectively. $\Re[\cdot]$ denotes the real part and the sum in Eq. (12) excludes terms for which $\lambda_r + \lambda_s = 0$. The computation of the time-dependent QFI of ρ_L at time t is explained in SM S1.

Quantum Fisher information analysis. To quantify the sensitivity of our probe for inferring h_1, one can use the QFI of ρ_L for different block sizes. In Fig. 2a–d, we plot the dynamics of QFI, $F_Q(t)$, as a function of time $t = n\tau$, for different values of h_1 when h_0 is tuned at $h_0/J = 1$. Each panel in Fig. 2a–d represents a different block size namely: (a) $L = 1$, (b) $L = 2$, (c) $L = 4$, and (d) $L = 10$. The QFI shows oscillatory behavior with damping amplitudes which at long times saturates to a steady state value depending on h_1. The steady state QFI value becomes significantly larger as the block size L increases, implying that the sensing precision considerably enhances as L increases. The long-time oscillations in the QFI persist because of the finite total system size N. To obtain the steady state value, we consider time averaged QFI given by

$$F_Q^{ss} = \frac{1}{\tau(n_{max} - n_{min})} \sum_{t=n_{min}\tau}^{n_{max}\tau} F_Q(t). \tag{13}$$

Typically, for our numerical calculation, n_{min} and n_{max} are taken to be 4000 and 4400, respectively for Fig. 2. These values are chosen to include a few oscillations of $F_Q(t)$. Once this condition is satisfied, any further widening of the range of n_{min} and n_{max} will give almost the same value of F_Q^{ss}. In fact, one can take the limit $n \to \infty$ and obtained $F_Q^{ss} = \lim_{n\to\infty} F_Q(n\tau)$ for the state ρ_L. To do this, we note that

$$U_k(n\tau) = e^{-i\mu_k^{F,+}n\tau}|\mu_k^{F,+}\rangle\langle\mu_k^{F,+}| + e^{-i\mu_k^{F,-}n\tau}|\mu_k^{F,-}\rangle\langle\mu_k^{F,-}|, \tag{14}$$

where, $\mu_k^{F,\pm}, |\mu_k^{F,\pm}\rangle$ are the eigenvalues and eigenvectors of the Floquet Hamiltonian, respectively. Then the expectation value of $\mathscr{C}_{i,j}(n\tau) = \langle\Psi(n\tau)|c_i^\dagger c_j|\Psi(n\tau)\rangle$ and $\mathscr{I}_{i,j}(n\tau) = \langle\Psi(n\tau)|c_i^\dagger c_j^\dagger|\Psi(t)\rangle$ between the fermionic operators $(i,j = 1,\ldots,L)$ can be obtained as

$$\begin{aligned}
\mathscr{C}_{i,j}(n\tau) =& \frac{2}{N}\sum_{k>0}\cos(k(i-j))\langle\psi_k^0|U_k^\dagger(n\tau)d_k^\dagger d_k U_k(n\tau)|\psi_k^0\rangle \\
=& \frac{2}{N}\sum_{k>0}\cos(k(i-j))\Big[r_k^+ r_k^{*+}\langle\mu_k^{F,+}|d_k^\dagger d_k|\mu_k^{F,+}\rangle \\
&+ r_k^- r_k^{*-}\langle\mu_k^{F,-}|d_k^\dagger d_k|\mu_k^{F,-}\rangle \\
&+ e^{i(\mu_k^{F,+}-\mu_k^{F,-})n\tau} r_k^+ r_k^{*-}\langle\mu_k^{F,+}|d_k^\dagger d_k|\mu_k^{F,-}\rangle \\
&+ e^{i(\mu_k^{F,-}-\mu_k^{F,+})n\tau} r_k^- r_k^{*+}\langle\mu_k^{F,-}|d_k^\dagger d_k|\mu_k^{F,+}\rangle\Big].
\end{aligned} \tag{15}$$

$$\begin{aligned}
\mathscr{I}_{i,j}(t) =& \frac{2i}{N}\sum_{k>0}\sin(k(i-j))\langle\psi^0|U_k^\dagger(n\tau)d_k^\dagger d_{-k}^\dagger U_k()n\tau|\psi^0\rangle \\
=& \frac{2i}{N}\sum_{k>0}\sin(k(i-j))\Big[r_k^+ r_k^{*+}\langle\mu_k^{F,+}|d_k^\dagger d_{-k}^\dagger|\mu_k^{F,+}\rangle \\
&+ r_k^- r_k^{*-}\langle\mu_k^{F,-}|d_k^\dagger d_{-k}^\dagger|\mu_k^{F,-}\rangle \\
&+ e^{i(\mu_k^{F,+}-\mu_k^{F,-})n\tau} r_k^+ r_k^{*-}\langle\mu_k^{F,+}|d_k^\dagger d_{-k}^\dagger|\mu_k^{F,-}\rangle \\
&+ e^{i(\mu_k^{F,-}-\mu_k^{F,+})n\tau} r_k^- r_k^{*+}\langle\mu_k^{F,-}|d_k^\dagger d_{-k}^\dagger|\mu_k^{F,+}\rangle\Big].
\end{aligned} \tag{16}$$

Here, $r_k^\pm = \langle\psi_k^0|\mu_k^{F,\pm}\rangle$, describes the overlap of the initial state with that of the Floquet eigenstates. Taking the limit $n \to \infty$ and $N \to \infty$, it is compatible to drop the fast oscillating cross-term from Eqs. (15–16). Thus, we obtain the correlation functions in the steady-state as

$$\begin{aligned}
\mathscr{C}_{i,j}^{\infty} =& \frac{1}{\pi}\int_0^\pi dk\cos(k(i-j))\Big[|r_k^+|^2\langle\mu_k^{F,+}|d_k^\dagger d_k|\mu_k^{F,+}\rangle \\
&+ |r_k^-|^2\langle\mu_k^{F,-}|d_k^\dagger d_k|\mu_k^{F,-}\rangle\Big],
\end{aligned} \tag{17}$$

$$\begin{aligned}
\mathscr{I}_{i,j}^{\infty} =& \frac{i}{\pi}\int_0^\pi dk\sin(k(i-j))\Big[|r_k^+|^2\langle\mu_k^{F,+}|d_k^\dagger d_{-k}^\dagger|\mu_k^{F,+}\rangle \\
&+ |r_k^-|^2\langle\mu_k^{F,-}|d_k^\dagger d_{-k}^\dagger|\mu_k^{F,-}\rangle\Big],
\end{aligned} \tag{18}$$

where we replace the summation by integration. The $C_{i,j}^{\infty}$ and $\mathscr{I}_{i,j}^{\infty}$ obtained so characterize a steady-state reduced density matrix ρ_L. The reduced density matrix is diagonalized in the orthogonal basis $\{|\mu_k^{F,\pm}\rangle\}$ which can be described by a time-periodic generalized canonical ensemble[82,83]. This state can be used to compute the Fisher information in Eq. (13), as described in details in the SM S1.

One of the main advantages of our quantum-many body probes is the presence of another external parameter, namely the DC field h_0, which can be tuned to enhance the sensing precision. To see the effect of h_0 on the steady state QFI, in Fig. 3a–d, we plot F_Q^{ss} as a function of both h_0 and h_1 for different block sizes namely: (a) $L = 1$; (b) $L = 2$; (c) $L = 4$; and (d) $L = 10$. As evident in the figures, by increasing the block size L, the F_Q^{ss} increases considerably and peaks along a line in the plane of h_0−h_1. It is shown in[84,85], that the steady-state properties of periodically driven systems are closely linked to the spectrum of the Floquet Hamiltonian. Especially, it is shown that at the Floquet band crossing several peaks occur in the entanglement entropy. To understand the origin of peaks in the F_Q^{ss} in the present case, we fix τ and analyze the Floquet gap Δ_F as a function of h_1 and h_0. The Δ_F is defined as

$$\Delta_F = \min_k(2|\vec{\mu}_k^F|), \tag{19}$$

namely, the minimum gap between the two Floquet bands, $\mu^{F,+} = |\vec{\mu}_k^F|$ and $\mu^{F,-} = -|\vec{\mu}_k^F|$. The $|\vec{\mu}_k^F|$ depends on h_0, h_1, and τ. For a fixed τ, h_0, and h_1, the minimum of $|\vec{\mu}_k^F|$ occurs at $k = \pi$. Thus, $\vec{\mu}_k^i$ becomes $\vec{\mu}_{k=\pi}^i = (0,0,h_0 - J)$ which using Eq. (7) gives $\cos(|\vec{\mu}_{k=\pi}^F|\tau) = \cos((h_0 - J)\tau + Jh_1)$. For certain values of h_0 and

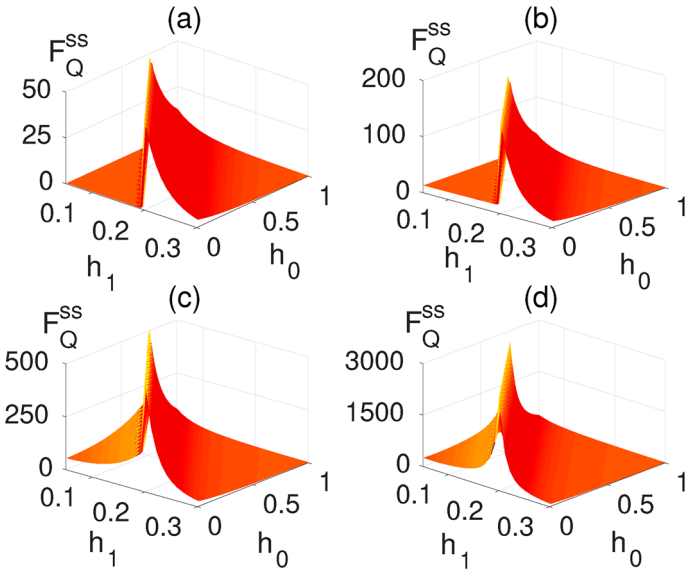

Figure 3. Variation of average long-time quantum Fisher information F_Q^{ss} with respect to h_1 and h_0 for different block sizes: (**a**) $L = 1$; (**b**) $L = 2$; (**c**) $L = 4$; and (**d**) $L = 10$. For the numerical calculation of quantum Fisher information, we choose $dh_1 = 10^{-3}$, see Eq. (12). Here $N = 2000$ and $J\tau = 0.2$.

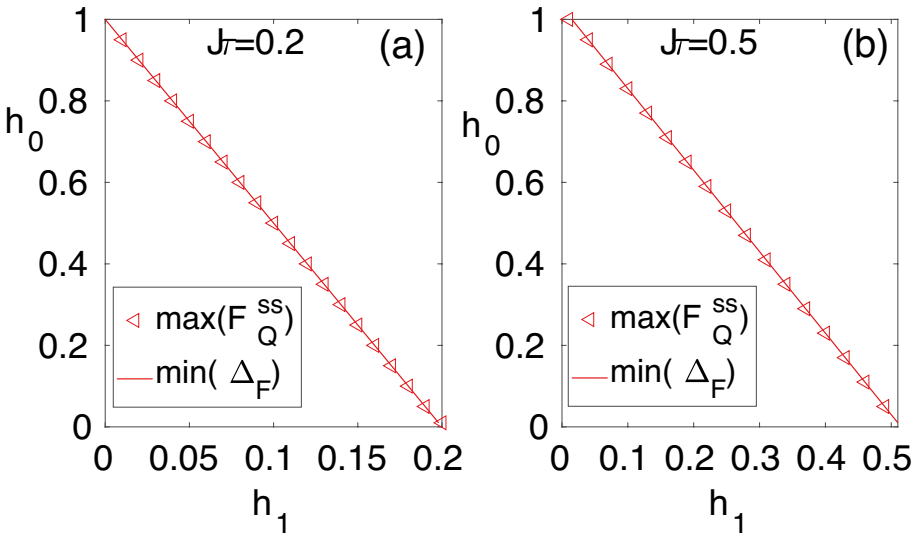

Figure 4. The minimum of the Floquet gap Δ_F (red regular line) and the peak value of quantum Fisher information F_Q^{ss} (red triangles) on the h_0−h_1 plane for: (**a**) $J\tau = 0.2$; and (**b**) $J\tau = 0.5$. Here, the total system size is $N = 2000$ and the block size is $L = 4$.

h_1, it can be checked that $|\vec{\mu}_\pi^F| = 0$. Thus, for those value of h_0 and h_1, the Floquet band gap $\Delta_F = 0$. By solving the former equation for $\vec{\mu}_{k=\pi}^F = 0$, we get

$$Jh_1 = \tau|h_0 - h_c|. \tag{20}$$

Interestingly, we find that for a fixed τ the peaks of F_Q^{ss} occur along a straight line in the h_0−h_1 plane where the Floquet gap Δ_F vanishes. In Fig. 4a,b we plot the location of points in the h_1−h_0 plane where Δ_F is minimum and F_Q^{ss} is maximum. The two lines perfectly collapse on each other showing that the vanishing Floquet gap corresponds to the maximum of the steady state QFI for various choices of τ. This resembles the correspondence between the closing of the energy gap at the critical point and the maximization of the QFI in the ground state quantum sensing with global accessibility.

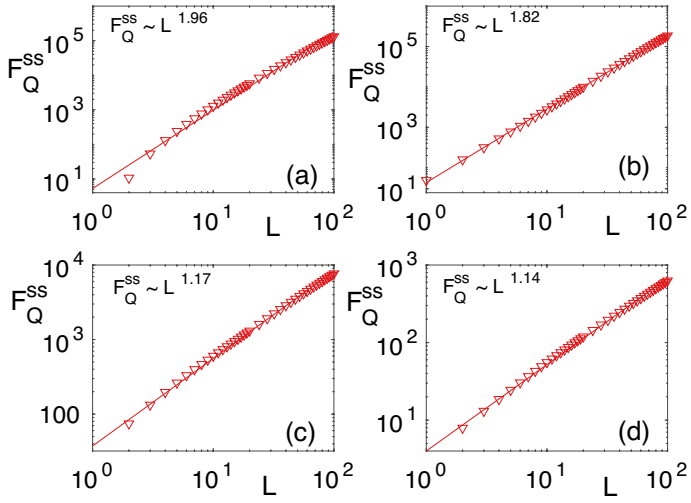

Figure 5. Quantum Fisher information F_Q^{ss} versus the block size L in a system of length $N = 10^4$ and time period of $J\tau = 0.2$: (**a**) $(h_0/J, h_1/J) = (0.191, 0.161)$; (**b**) $(h_0/J, h_1/J) = (0.83, 0.034)$; (**c**) $(h_0/J, h_1/J) = (0.161, 0.191)$; and (**d**) $(h_0/J, h_1/J) = (0.6, 0.2)$. The plots in panels (**a**) and (**b**) belong to the vanishing Floquet gap line while the panels (**c**) and (**d**) are away from that. The triangles represent original numerical data while the solid red lines are the fitting curve using the least-square method.

Steady state scaling of quantum Fisher information. One important features of quantum sensing in comparison with classical methods is resource efficiency. This is quantified through scaling of the QFI with respect to the number of resources needed to perform the estimation. In our setup, we have access to spins in a block of size L which is explained by the density matrix ρ_L. Since all the measurements will be performed on this block, it is reasonable to consider the number of spins L as the resource for our quantum sensing protocol. To quantify the effectiveness of our steady state sensing protocol, one has to investigate the scaling of F_Q^{ss} as a function of resources L. Therefore, by fixing h_0 and h_1, one can explore how F_Q^{ss} (which is computed with respect to h_1) changes with increasing L. In particular, we fit the numerical data with the fitting function of the form $f(L) = AL^{\eta}$ such that for every choice of pair (h_0, h_1), one gets $F_Q^{ss} \approx f(L)$. In general, $A(h_0, h_1)$ and $\eta(h_0, h_1)$ are functions of h_0 and h_1. The exponent $\eta = 1$ corresponds to the classical standard limit and any $\eta > 1$ shows quantum enhanced sensing, with $\eta = 2$ being the Heisenberg limit. In Fig. 5a, we fix $(h_0/J, h_1/J) = (0.191, 0.161)$ which corresponds to one point along the line with vanishing Floquet gap where the QFI is maximum. Surprisingly, by considering block sizes of $L = 1-100$, the steady state QFI shows scaling with $F_Q^{ss} \sim L^{1.96}$, which is well beyond the standard limit. In Fig. 5b, we take $(h_0, h_1) = (0.83, 0.034)$ as another point on the vanishing Floquet gap line where the fitting gives $F_Q^{ss} \sim L^{1.82}$, which again shows quantum enhanced sensing. For the sake of completeness, in Fig. 5c,d, we plot F_Q^{ss} versus block size L for the two representative pairs of $(h_0, h_1) = (0.161, 0.191)$ and $(h_0, h_1) = (0.6, 0.2)$ away from the vanishing Floquet gap line. Interestingly, for these choices, although η still exceeds the standard limit, it is considerably smaller than the choices of the points on the vanishing Floquet gap line. These findings are the key results of this paper and are analogous to the enhanced sensitivity near the ground state critical point[51,50], where the energy gap of the system vanishes. As criticality is a resource for ground state quantum sensing, the vanishing of the Floquet gap can also be considered a resource for steady state quantum metrology.

It is worth emphasizing that there is a fundamental difference between our protocol and the conventional criticality enhanced sensitivity in the ground state of many-body systems. In such scenarios, the Fisher information is computed for the whole system assuming global accessibility. In our case, while the whole system remains a pure state, the local subsystem becomes mixed due to entanglement with the rest of the system. Due to this mixedness, some information may get lost and sensing is more challenging. Nonetheless, our analysis shows that in integrable systems the local steady state still carries a wealth of information about the AC field allowing for sensitivity near the Heisenberg limit. This is non-trivial as, for instance, in GHZ-based quantum sensing[37,38] even losing one particle completely destroys the quantumness of the probe.

We would like to mention that the scaling analysis carried out in this section is robust with the increase of the total system size N. We have considered N in the range of $N = 2000$ to $N = 10000$ for which the value of the scaling exponent η remains pretty much robust as shown in Fig. 5a–d. Moreover, the scaling exponents have been extracted for $L = 1-100$ as further increasing the block size L hardly changes the fitting function and the exponent η.

Role of the initial state. In this section, we discuss the role of the initial state for the estimation of h_1. For this, in Fig. 6a, we plot the steady-state magnetization m_z^{ss} as a function of h_1 for two different initial states, namely: (i) ordered state $|\Psi(0)\rangle = |\rightarrow \otimes \rightarrow \otimes \cdots \otimes \rightarrow\rangle$ (with $|\rightarrow\rangle = (|\uparrow\rangle + |\downarrow\rangle)/\sqrt{2}$); and (ii) disordered state $|\Psi(0)\rangle = |\uparrow \otimes \uparrow \otimes \cdots \otimes \uparrow\rangle$. For both of these cases, the m_z^{ss} starts from its initial value at $h_1 = 0$ and saturates for large h_1. The slope of m_z^{ss} at any h_1 captures the degree of sensitivity for a small change on h_1, which

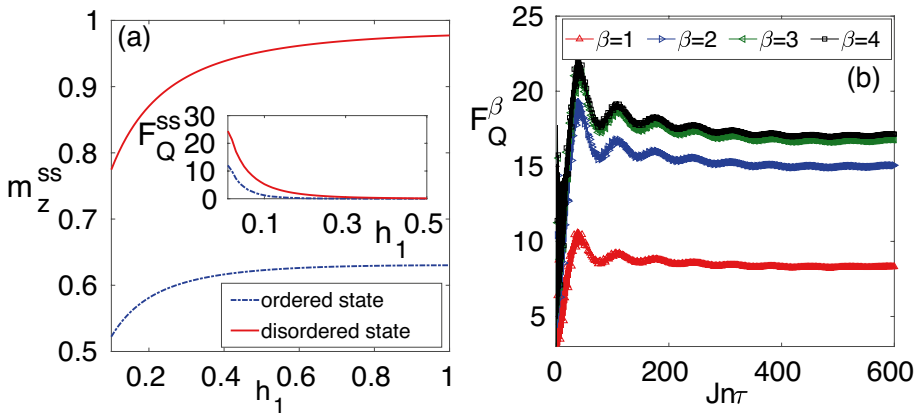

Figure 6. (**a**) The variation of the steady-state magnetization as a function of h_1 for disordered and ordered initial states, respectively. The corresponding steady-state QFI is shown in the inset. (**b**) The QFI (F_Q^β) of a block of size $L = 2$ as a function of time $t = n\tau$ for a thermal initial state at the finite temperature $T = \frac{1}{\kappa\beta}$. Here, $(h_0/J, h_1/J) = (0.191, 161)$, $J\tau = 0.2$, and $N = 2000$.

in turn gives the information about h_1 that can be obtained from the measurement of m_z^{ss}. In the inset of Fig. 6a, we plot F_Q^{ss} for the two different initial states. It is clear from the figure that the QFI takes larger values for the disordered initial state.

In order to consider a mixed initial state, we explore the performance of our AC field quantum sensing for a thermal initial state too. For this, the system is prepared initially in a thermal state $\rho = e^{-\beta H_0}/\mathscr{Z}$, where $\mathscr{Z} = \mathrm{Tr}\,(e^{-\beta H_0})$ is the normalization constant and H_0 is the time-independent Hamiltonian, namely the Hamiltonian in Eq. (1) without the term $h(t)$. The subsequent dynamics can be obtained as $\rho(t) = U(t)\rho U^\dagger(t)$, where $U(t)$ is a unitary operator given in Eq. (3). We obtain a reduced density matrix between two-spins, i.e., $L = 2$, and calculate the quantum Fisher information F_Q^β as a function of time $t = n\tau$. In Fig. 6b, we plot F_Q^β as a function of time for different $\beta = 1/\kappa T$, where T is the temperature of the system and κ is the Boltzmann constant. Here, we have taken the values of $h_0/J = 0.191$ and $h_1/J = 0.161$ which corresponds to the point where Floquet gap Δ_F vanishes and F_Q^{ss} shows a peak. From Fig. 6b, it can be seen that by increasing β (decreasing temperature T), the F_Q^β increases. Thus, we can infer that the uncertainty in the estimation of h_1 increases as the temperature increases. However, from Fig. 6b it is clear that $F_Q^\beta \gg 1$, one can still get significant precision in the estimation of h_1 even at the finite temperature β.

Realization on near-term quantum devices. Near-term quantum devices are far from being perfect. They have several limitations in terms of the number of qubits, measurement types, and coherence time. In addition, realizing a perfectly integrable system is challenging. We particularly, focus on ion trap systems in which the interaction between the qubits is described by the Hamiltonian[86–90]

$$H_\alpha(t) = -\sum_{i,j} \frac{J}{r_{ij}^\alpha}\hat{\sigma}_i^x\hat{\sigma}_j^x - \sum_i (h_0 + h(t))\hat{\sigma}_i^z, \tag{21}$$

where α determines the strength of interaction between sites i and j and can be tuned experimentally. The case of $\alpha = 0$ describes a fully connected graph in which all qubits interact with each other equally. On the other hand, in the limit of $\alpha \to \infty$ one recovers the integrable Hamiltonian as in Eq. (1). In general, for finite values of α, the above Hamiltonian is non-integrable. However, as α increases the non-integrability becomes weaker such that for $\alpha > 1$ system behaves more like the nearest neighbor Ising model. In typical ion trap experiments, α varies in the range $0.5 \le \alpha \le 3$, the coupling strength J is in the range $J \in [10^2, 10^4]$ Hz, and the coherence time $T_2 \ge 10^{-3}$ s[91]. We consider a system of size $N = 13$ with $\alpha = 3$. As we will see, such small systems with $\alpha = 3$, despite being non-integrable, still do not reach the infinite temperature thermal state for their subsystems. Therefore, one can still efficiently use them for steady state sensing within the coherence time of the system.

Since the optimal measurement basis is complex and in general h_1 dependent, we suggest using the non-optimal but simple block magnetization measurement, described in the previous section. For such measurement, one can compute the classical Fisher information and compare it with the QFI. In Fig. 7a,b we plot both the CFI and QFI as a function of time in a system of length $N = 13$, $(h_0, h_1) = (0.191, 0.161)$, and $L = 4$ for: (a) $\alpha \to \infty$; and (b) $\alpha = 3$, respectively. Interestingly, despite being non-integrable, the system shows very large classical and quantum Fisher information. In addition, the system reaches its steady state around $nJ\tau = 100$. For a typical exchange coupling of $J \sim 10$ KHz[92], one needs a coherence time of ~ 10 ms. This is within the capability of current ion trap technologies which have achieved coherence time of 300 ms (extendable to 2.1 s with dynamical decoupling)[93].

Any quantum sensing protocol requires an estimation algorithm which uses the measured data for estimating the unknown parameter. Indeed, only by using an optimal estimation algorithm, together with optimal measurements, one can saturate the Cramér–Rao bound. Bayesian estimation is known to be the optimal estimator[94–98] for

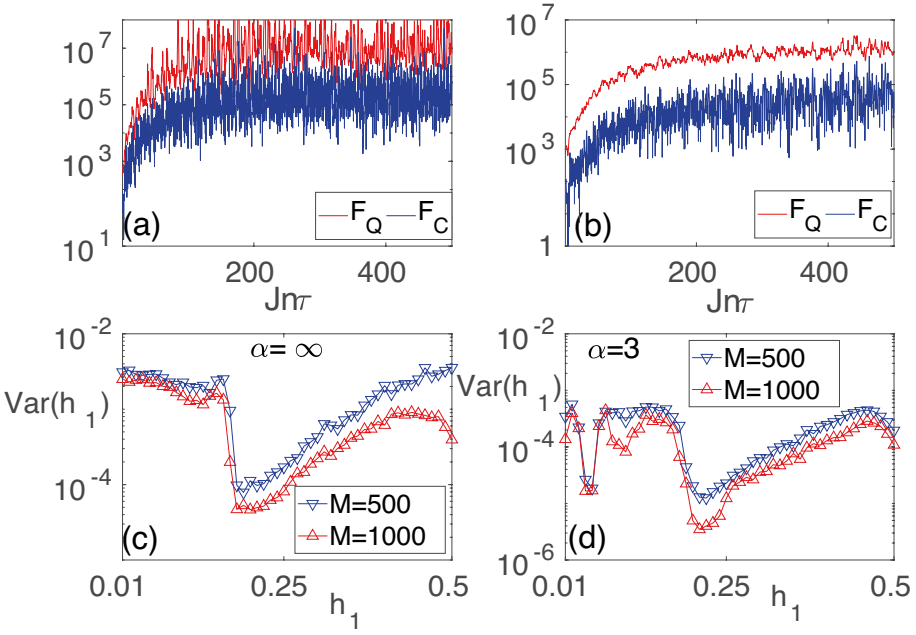

Figure 7. The evolution of F_Q and F_C as a function of time when $(h_0/J, h_1/J) = (0.191, 0.161)$ are tuned to be on the line of the vanishing Floquet gap for: (**a**) $\alpha \to \infty$; and (**b**) $\alpha = 3$. The variance $\mathrm{Var}(h_1)$ in the estimation of h_1 using Bayesian inference for two different numbers of repetitions M for: (**c**) $\alpha \to \infty$; and (**d**) $\alpha = 3$. The other parameters are $N = 13$, $J\tau = 0.2$, and $L = 4$.

large data sets. In SM S1, we presented optimal measurement basis for $L = 1$ and $L = 2$ for the Hamiltonian given in Eq. (1). The optimal measurement basis so obtained cannot be generalized to higher L due to the complexity involved. Thus, we restore to a simple measurement which can be accessible in experiments. Consider block magnetization measurement which results in a data set of M samples $\mathbf{d} = \{(O_k, n_k)\}$, in which any measurement outcome O_k appears n_k times (with $k = 1, 2, \ldots, L+1$) such that $\sum_k n_k = M$. The probability distribution of the unknown parameter h_1 is determined as

$$\mathbb{P}(h_1|\mathbf{d}) = \frac{\mathbb{P}(\mathbf{d}|h_1)\mathbb{P}(h_1)}{\mathbb{P}(\mathbf{d})}, \tag{22}$$

where, $\mathbb{P}(h_1|\mathbf{d})$ is the posterior, $\mathbb{P}(\mathbf{d}|h_1)$ is the likelihood, $\mathbb{P}(h_1)$ is the prior probability distribution of h_1, and $\mathbb{P}(\mathbf{d})$ is the normalization factor to make the posterior a valid probability distribution. In the absence of prior information, one can consider $\mathbb{P}(h_1)$ to be a uniform distribution over the interval of interest. The likelihood can be computed as

$$\mathbb{P}(\mathbf{d}|h_1) = \binom{M}{n_1, n_2, \ldots, n_{L+1}} \prod_{k=1}^{L+1} (p_k)^{n_k}, \tag{23}$$

where, p_k is the probability of measuring outcome O_k. The estimated value h_1^{est} is the point at which the posterior $\mathbb{P}(h_1|\mathbf{d})$ takes its maximum. By repeating the procedure one can estimate the variance $\mathrm{Var}(h_1)$. Using block magnetization measurement, in Fig. 7c,d, we plot the variance as a function of h_1 in a system of length $N = 13$, block size $L = 4$ for: (a) $\alpha \to \infty$; and (b) $\alpha = 3$. The variance remains below 10^{-2} throughout the considered interval. As expected, by increasing the sample size M the variance decreases.

Effect of the total system size. So far, we have considered the situation in which the total system size is much larger than the subsystem of interest, namely $L \ll N$. This implies that the subsystem reaches its equilibrium and thus the reduced density matrix does not fluctuate in time which makes the sensing easier. However, current quantum devices are still very limited in terms of the number of qubits. Thus, it is important to see the performance of our protocol for fairly small total system sizes. In Fig. 8a,b, we plot the F_Q for a block of size $L = 4$ and different system sizes N as a function of time $t = n\tau$ for: (a) $(h_0, h_1) = (0.191, 0.161)$; and (b) $(h_0, h_1) = (0.6, 0.2)$, respectively. The first choices of h_0 and h_1 are chosen along the peak of the F_Q^{ss} whereas the second one away from the peak. Interestingly, the QFI takes much larger values for the smaller system sizes which make sensing even more efficient. This is because in small systems the L/N ratio is larger and there are fewer degrees of freedom over which the information is dispersed. As a result, the reduced density matrix ρ_L contains more information about h_1 which reveals itself in larger values of the QFI. At the same time, since the

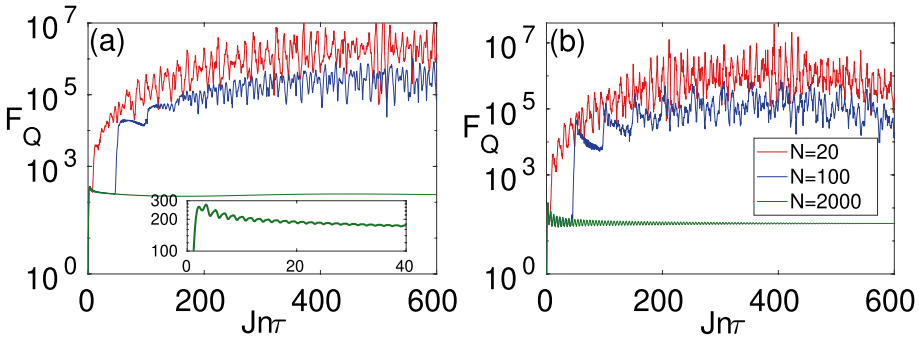

Figure 8. Dynamics of F_Q as a function of time $t = n\tau$ for various total system sizes and the time period $J\tau = 0.2$: (**a**) $h_0/J = 0.191, h_1/J = 0.161$; and (**b**) $h_0/J = 0.6, h_1/J = 0.2$. Here $L = 4$.The inset in (**a**) show the behavior of F_Q in small time scale i.e., $t \approx 40/J$.

total system size is smaller, the QFI shows more fluctuations for small systems which is a sign of a lack of full equilibration.

Role of integrability. The proposed protocol is very general and can be applied to any integrable time-independent Hamiltonian. In case of a non-integrable Hamiltonian, the periodic magnetic field leads to the heating phenomena[76,99]. Due to this heating effect, the long-time steady state is an infinite temperature state. Such an infinite temperature state no longer remains sensitive to the magnetic field h_1. Therefore, a non-integrable quantum sensor may not be useful for many-body steady state AC field quantum sensing. On the other hand, it is known that in integrable models under a periodic perturbation, the observable syncronize with the driving and do not heat up[85,100].

The dynamics of many-body system under periodic driving at the *stroboscopic* time can be described by Floquet Hamiltonian H^F. For small $J\tau$, the Floquet Hamiltonian H^F can be approximated by average Hamiltonian $H_{ave} = 1/\tau \int_0^\tau H(t)dt$, i.e., $H^F \approx H_{ave}$. For arbitrary τ, the Floquet Hamiltonian is given by the Floquet-Magnus expansion. In Ref.[99], it is shown that in generic integrable spin models the Floquet-Magnus expansion diverges around $J\tau \approx 1$, i.e. H^F becomes infinite, which results in the sudden increase in the energy of the H_{ave}. This means that for $J\tau > 1$ even integrable systems can reach to infinite temperature state in their subsystems. For general Hamiltonians the sufficient condition for the convergence of Floquet-Magnus expansion is $J\tau \leq 1/||H(t)||$, where $||.||$ is the operator norm. This means that in our model for $J\tau < 1$, the long-time steady state is different from the infinite temperature state. It is this feature of integrability that is used in the present sensing protocol.

Note that the above argument does not necessarily mean that non-integrable systems cannot be used for steady state sensing at all. In fact, reaching the infinite temperature state requires large total system size N and exponentially long time scales[99,101–104], in particular, if the non-integrability is weak. This very slow equilibration gives opportunity for quantum sensing before the system reaches the infinite temperature steady state. This is a crucial fact as, in practice, perfectly integrable systems might be difficult to realize.

While, for the simplicity of the numerics, we mainly focus on the Dirac-delta AC field, the procedure is general and was used to infer the amplitude of a square AC field too (see the SM S1). We also discussed the main merit of our protocol over the existing one in the SM S1.

Discussion and conclusion

In this paper, we showed that the Ising model in a transverse field, as an integrable model, can be used for detecting the amplitude of an AC field. To enhance the precision of the estimation a controllable DC transverse field is also applied. By the combination of analytical and numerical simulation, based on Floquet formalism, we compute the quantum Fisher information of a block of spins when their reduced density matrix saturates to the steady state. We have four main results: (i) in contrary to the conventional spin-echo and dynamical decoupling approaches, in which interaction between particles is not helpful, our approach harnesses such interactions for AC field sensing without demanding extra pulses; (ii) in clear distinction from the ground state critical sensing systems, our protocol only demands partial accessibility to the system; (iii) the steady state quantum Fisher information can reveal scaling beyond the standard limit, almost achieving the Heisenberg bound, with respect to the block size; and (iv) analytical analysis using the Floquet formalism, shows that this quantum enhanced scaling corresponds to the closing of the Floquet gap. Our results are general to all integrable systems in which Floquet heating does not occur. This means that the transverse Ising model can be used as a many-body sensor for all AC fields with $J\tau < 1$. However, we show that if the non-integrability is weak and the total system size is not very large, the non-integrable systems can still be used for efficient sensing too. Moreover, we have considered block magnetization as a simple, though sub-optimal, measurement basis that can be used in practice for efficient sensing. The resulting classical Fisher information is fairly close to the QFI, as the ultimate precision bound. Block magnetization measurement together with the Bayesian estimation algorithm have been used for quantum sensing to show the practicality of the protocol in near-term quantum simulators, such as the ion-traps.

Received: 22 November 2021; Accepted: 25 July 2022
Published online: 30 August 2022

References

1. Degen, C. L., Reinhard, F. & Cappellaro, P. Quantum sensing. *Rev. Mod. Phys.* **89**, 035002 (2017).
2. Kominis, I. K., Kornack, T. W., Allred, J. C. & Romalis, M. V. A subfemtotesla multichannel atomic magnetometer. *Nature* **422**, 596 (2003).
3. Budker, D. & Romalis, M. Optical magnetometry. *Nat. Phys.* **3**, 227 (2007).
4. Vengalattore, M. *et al.* High-resolution magnetometry with a spinor bose-einstein condensate. *Phys. Rev. Lett.* **98**, 200801 (2007).
5. Taylor, J. M. *et al.* High-sensitivity diamond magnetometer with nanoscale resolution. *Nat. Phys.* **4**, 810 (2008).
6. Kitching, J., Knappe, S. & Donley, E. A. Atomic sensors: A review. *IEEE Sensors J.* **11**, 1749 (2011).
7. Bal, M., Deng, C., Orgiazzi, J.-L., Ong, F. R. & Lupascu, A. Ultrasensitive magnetic field detection using a single artificial atom. *Nat. Commun.* **3**, 1324 (2012).
8. Kornack, T. W., Ghosh, R. K. & Romalis, M. V. Nuclear spin gyroscope based on an atomic comagnetometer. *Phys. Rev. Lett.* **95**, 230801 (2005).
9. Morello, A. *et al.* Single-shot readout of an electron spin in silicon. *Nature* **467**, 687 (2010).
10. Sedlacek, J. A. *et al.* Microwave electrometry with rydberg atoms in a vapour cell using bright atomic resonances. *Nat. Phys.* **8**, 819 (2012).
11. Brownnutt, M., Kumph, M., Rabl, P. & Blatt, R. Ion-trap measurements of electric-field noise near surfaces. *Rev. Mod. Phys.* **87**, 1419 (2015).
12. Fan, H. *et al.* Atom based RF electric field sensing. *J. Phys. B: At. Mol. Opt. Phys.* **48**, 202001 (2015).
13. Schnabel, R., Mavalvala, N., McClelland, D. E. & Lam, P. K. Quantum metrology for gravitational wave astronomy. *Nat. Commun.* **1**, 121 (2010).
14. Lovchinsky, I. *et al.* Magnetic resonance spectroscopy of an atomically thin material using a single-spin qubit. *Science* **355**, 503 (2017).
15. Jensen, K. *et al.* Non-invasive detection of animal nerve impulses with an atomic magnetometer operating near quantum limited sensitivity. *Sci. Rep.* **6**, 29638 (2016).
16. McGuinness, L. P. *et al.* Quantum measurement and orientation tracking of fluorescent nanodiamonds inside living cells. *Nat. Nanotechnol.* **6**, 358 (2011).
17. Timoney, N. *et al.* Quantum gates and memory using microwave-dressed states. *Nature* **476**, 185 (2011).
18. Baumgart, I., Cai, J.-M., Retzker, A., Plenio, M. B. & Wunderlich, Ch. Ultrasensitive magnetometer using a single atom. *Phys. Rev. Lett.* **116**, 240801 (2016).
19. Weidt, S. *et al.* Trapped-ion quantum logic with global radiation fields. *Phys. Rev. Lett.* **117**, 220501 (2016).
20. Lang, J. E., Liu, R. B. & Monteiro, T. S. Dynamical-decoupling-based quantum sensing: Floquet spectroscopy. *Phys. Rev. X* **5**, 041016 (2015).
21. Khodjasteh, K. & Lidar, D. A. Fault-tolerant quantum dynamical decoupling. *Phys. Rev. Lett.* **95**, 180501 (2005).
22. Shor, P. W. Algorithms for quantum computation: discrete logarithms and factoring. In *Proceedings 35th Annual Symposium on Foundations of Computer Science*. IEEE Comput. Soc. Press., 124 (1994)
23. de Lange, G., Ristè, D., Dobrovitski, V. V. & Hanson, R. Single-spin magnetometry with multipulse sensing sequences. *Phys. Rev. Lett.* **106**, 080802 (2011).
24. Hall, L. T., Cole, J. H., Hill, C. D. & Hollenberg, L. C. L. Sensing of fluctuating nanoscale magnetic fields using nitrogen-vacancy centers in diamond. *Phys. Rev. Lett.* **103**, 220802 (2009).
25. Schoenfeld, R. S. & Harneit, W. Real time magnetic field sensing and imaging using a single spin in diamond. *Phys. Rev. Lett.* **106**, 030802 (2011).
26. Rondin, L. *et al.* Magnetometry with nitrogen-vacancy defects in diamond. *Rep. Prog. Phys.* **77**, 056503 (2014).
27. Schirhagl, R., Chang, K., Loretz, M. & Degen, C. L. Nitrogen-vacancy centers in diamond: Nanoscale sensors for physics and biology. *Annu. Rev. Phys. Chem.* **65**, 83 (2014) (**PMID: 24274702**).
28. Paris, M. G. A. Quantum estimation for quantum Technology. *Int. J. Quant. Inf.* **07**, 125 (2009).
29. Abraham, R. J. Principles of magnetic resonance c. p. slichter. springer, berlin, 1990, ISBN 3 540 5057 6, 640 pages, DM89.00.. *Magn. Reson. Chem.* **28**, 1078 (1990).
30. Müller, T. *et al.* Optical signatures of silicon-vacancy spins in diamond. *Nat. Commun.* **5**, 3328 (2014).
31. Hansom, J. *et al.* Environment-assisted quantum control of a solid-state spin via coherent dark states. *Nat. Phys.* **10**, 725 (2014).
32. Acosta, V. M. *et al.* Diamonds with a high density of nitrogen-vacancy centers for magnetometry applications. *Phys. Rev. B* **80**, 115202 (2009).
33. Zhou, H., Choi, J., Choi, S., Land R., Douglas, A. M., Isoya, J., Jelezko, F., Onoda, S., Sumiya, H., Cappellaro, P., Knowles, H. S., Park, H., & Lukin. M. D. Quantum metrology with strongly interacting spin systems. *Phys. Rev. X* **10**, 031003 (2020).
34. Braunstein, S. L. & Caves, C. M. Statistical distance and the geometry of quantum states. *Phys. Rev. Lett.* **72**, 3439 (1994).
35. Liu, J., Yuan, H., Lu, X. M. & Wang, X. Quantum fisher information matrix and multiparameter estimation. *J. Phys. A: Math. Theor.* **53**, 023001 (2019).
36. Meyer, J. J. Fisher Information in Noisy Intermediate-Scale Quantum Applications. *Quantum* **5**, 539 (2021).
37. Giovannetti, V., Lloyd, S. & Maccone, L. Quantum metrology. *Phys. Rev. Lett.* **96**, 160501 (2006).
38. Cable, H. & Dowling, J. P. Efficient generation of large number-path entanglement using only linear optics and feed-forward. *Phys. Rev. Lett.* **99**, 163604 (2007).
39. Dür, W., Vidal, G. & Cirac, J. I. Three qubits can be entangled in two inequivalent ways. *Phys. Rev. A* **62**, 062314 (2000).
40. Kołodyński, J. & Demkowicz-Dobrzański, R. Efficient tools for quantum metrology with uncorrelated noise. *New J. Phys.* **15**, 073043 (2013).
41. De Pasquale, A., Rossini, D., Facchi, P. & Giovannetti, V. Quantum parameter estimation affected by unitary disturbance Phys. *Rev. A* **88**, 052117 (2013).
42. Bonato, C. *et al.* Optimized quantum sensing with a single electron spin using real-time adaptive measurements. *Nat. Nanotechnol.* **11**, 247 (2016).
43. Said, R. S., Berry, D. W. & Twamley, J. Nanoscale magnetometry using a single-spin system in diamond. *Phys. Rev. B* **83**, 125410 (2011).
44. Higgins, B. L., Berry, D. W., Bartlett, S. D., Wiseman, H. M. & Pryde, G. J. Entanglement-free Heisenberg-limited phase estimation. *Nature* **450**, 393 (2007).
45. Berry, D. W. *et al.* How to perform the most accurate possible phase measurements. *Phys. Rev. A* **80**, 052114 (2009).
46. Higgins, B. L. *et al.* Demonstrating Heisenberg-limited unambiguous phase estimation without adaptive measurements. *New J. Phys.* **11**, 073023 (2009).
47. Danilin, S. *et al.* Quantum-enhanced magnetometry by phase estimation algorithms with a single artificial atom. *NPJ Quantum Inf* **4**, 29 (2018).
48. Shlyakhov, A. R. *et al.* Quantum metrology with a transmon qutrit. *Phys. Rev. A* **97**, 022115 (2018).

49. Gammelmark, S. & Mølmer, K. Fisher information and the quantum cramér-rao sensitivity limit of continuous measurements. *Phys. Rev. Lett.* **112**, 170401 (2014).
50. Zanardi, P., Paris, M. G. A. & Venuti, L. C. Quantum criticality as a resource for quantum estimation. *Phys. Rev. A* **78**, 042105 (2008).
51. Invernizzi, C., Korbman, M., Venuti, L. C. & Paris, M. G. A. Optimal quantum estimation in spin systems at criticality. *Phys. Rev. A* **78**, 042106 (2008).
52. Salvatori, G., Mandarino, A. & Paris, M. G. A. Quantum metrology in lipkin-meshkov-glick critical systems. *Phys. Rev. A* **90**, 022111 (2014).
53. Bina, M., Amelio, I. & Paris, M. G. A. Dicke coupling by feasible local measurements at the superradiant quantum phase transition. *Phys. Rev. E* **93**, 052118 (2016).
54. Boyajian, W. L., Skotiniotis, M., Dür, W. & Kraus, B. Compressed quantum metrology for the ising hamiltonian. *Phys. Rev. A* **94**, 062326 (2016).
55. Rams, M. M., Sierant, P., Dutta, O., Horodecki, P. & Zakrzewski, J. At the limits of criticality-based quantum metrology: Apparent super-Heisenberg scaling revisited. *Phys. Rev. X* **8**, 021022 (2018).
56. Mehboudi, M., Correa, L. A. & Sanpera, A. Achieving sub-shot-noise sensing at finite temperatures. *Phys. Rev. A* **94**, 042121 (2016).
57. Boixo, S. *et al.* Quantum-limited metrology with product states. *Phys. Rev. A* **77**, 012317 (2008).
58. Boixo, S. *et al.* Quantum metrology: Dynamics versus entanglement. *Phys. Rev. Lett.* **101**, 040403 (2008).
59. Boixo, S. *et al.* Quantum-limited metrology and Bose-Einstein condensates. *Phys. Rev. A* **80**, 032103 (2009).
60. Tacla, A. B., Boixo, S., Datta, A., Shaji, A. & Caves, C. M. Nonlinear interferometry with Bose-Einstein condensates. *Phys. Rev. A* **82**, 053636 (2010).
61. Kiukas, J., Yuasa, K. & Burgarth, D. Remote parameter estimation in a quantum spin chain enhanced by local control. *Phys. Rev. A* **95**, 052132 (2017).
62. Siôn Jones, G., Bose, S., & Bayat, A. Remote quantum sensing with Heisenberg limited sensitivity in many body systems. arXiv: 2003.02308 (2020).
63. Gühne, O., Tóth, G. & Briegel, H. J. Multipartite entanglement in spin chains. *New J. Phys.* **7**, 229 (2005).
64. Gühne, O. & Tóth, G. Energy and multipartite entanglement in multidimensional and frustrated spin models. *Phys. Rev. A* **73**, 052319 (2006).
65. Campbell, S. & Paternostro, M. Multipartite nonlocality in a thermalized ising spin chain. *Phys. Rev. A* **82**, 042324 (2010).
66. Giampaolo, S. M. & Hiesmayr, B. C. Genuine multipartite entanglement in the x y model. *Phys. Rev. A* **88**, 052305 (2013).
67. Giampaolo, S. M. & Hiesmayr, B. C. Genuine multipartite entanglement in the cluster-ising model. *New J. Phys.* **16**, 093033 (2014).
68. Bayat, A. Scaling of tripartite entanglement at impurity quantum phase transitions. *Phys. Rev. Lett.* **118**, 036102 (2017).
69. Dutta, A., Aeppli, G., Chakrabarti, B. K. Divakaran, U., Rosenbaum, T. F. & Sen, D. Quantum phase transitions. In *Quantum Phase Transitions in Transverse Field Spin Models*, 3–31. Cambridge University Press.
70. Sachdev, S. *Quantum Phase Transitions*. Cambridge University Press, (2009).
71. Raghunandan, M., Wrachtrup, J. & Weimer, H. High-density quantum sensing with dissipative first order transitions. *Phys. Rev. Lett.* **120**, 150501 (2018).
72. Roushan, P. *et al.* Spectroscopic signatures of localization with interacting photons in superconducting qubits. *Science* **358**, 1175 (2017).
73. Bayat, A., Alkurtass, B., Sodano, P., Johannesson, H. & Bose, S. Measurement quench in many-body systems. *Phys. Rev. Lett.* **121**, 030601 (2018).
74. Bayat, A., Bose, S., Johannesson, H. & Sodano, P. Universal single-frequency oscillations in a quantum impurity system after a local quench. *Phys. Rev. B* **92**, 155141 (2015).
75. Mishra, U. & Bayat, A. Driving enhanced quantum sensing in partially accessible many-body systems. *Phys. Rev. Lett.* **127**, 080504 (2021).
76. D'Alessio, L. & Rigol, M. Long-time behavior of isolated periodically driven interacting lattice systems. *Phys. Rev. X* **4**, 041048 (2014).
77. Lazarides, A., Das, A. & Moessner, R. Periodic thermodynamics of isolated quantum systems. *Phys. Rev. Lett.* **112**, 150401 (2014).
78. Thakurathi, M., Patel, A. A., Sen, D. & Dutta, A. Floquet generation of majorana end modes and topological invariants. *Phys. Rev. B* **88**, 155133 (2013).
79. Sieberer, L. M. *et al.* Digital quantum simulation, trotter errors, and quantum chaos of the kicked top. *NPJ Quantum Inf* **5**, 78 (2019).
80. Lieb, E., Schultz, T. & Mattis, D. Two soluble models of an antiferromagnetic chain. *Ann. Phys.* **16**, 407 (1961).
81. Barouch, E. & McCoy, B. M. Statistical mechanics of the XY model II spin-correlation functions. *Phys. Rev. A* **3**, 786 (1971).
82. Apollaro, T. J. G., Palma, G. M. & Marino, J. Entanglement entropy in a periodically driven quantum ising ring. *Phys. Rev. B* **94**, 134304 (2016).
83. Pappalardi, S. Russomanno, A. Silva, A. & Fazio, R. Multipartite entanglement after a quantum quench *J. Stat. Mech.* 053104 (2017).
84. Russomanno, A., Santoro, G. E. & Fazio, R. Entanglement entropy in a periodically driven ising chain. *J. Stat. Mech: Theory Exp.* **2016**, 073101 (2016).
85. Sen, A., Nandy, S. & Sengupta, K. Entanglement generation in periodically driven integrable systems: Dynamical phase transitions and steady state. *Phys. Rev. B* **94**, 214301 (2016).
86. Monroe, C., Campbell, W. C., Edwards, E. E., Islam, R., Kafri, D., Korenblit, S., Lee, A., Richerme, P., Senko, C., & Smith, J. Quantum Simulation of Spin Models with Trapped Ions, *Proceedings of the International School of Physics 'Enrico Fermi,' Course 189*, edited by M. Knoop, I. Marzoli, and G. Morigi, 169–187 (2015).
87. Cirac, J. I. & Zoller, P. Goals and opportunities in quantum simulation. *Nat. Phys.* **8**, 264 (2012).
88. Blatt, R. & Roos, C. F. Quantum simulations with trapped ions. *Nat. Phys.* **8**, 277 (2012).
89. Islam, R. *et al.* Emergence and frustration of magnetism with variable-range interactions in a quantum simulator. *Science* **340**, 583 (2013).
90. Britton, J. W. *et al.* Engineered 2D Ising interactions on a trapped-ion quantum simulator with hundreds of spins. *Nature***484**, 492 (2012).
91. Hazzard, K. R. A. *et al.* Quantum correlations and entanglement in far-from-equilibrium spin systems Phys. *Rev. A* **90**, 063622 (2014).
92. Monroe, C. *et al.* Programmable quantum simulations of spin systems with trapped ions. *Rev. Mod. Phys.* **93**, 25001 (2021).
93. Ruster, T. *et al.* A long-lived Zeeman trapped-ion qubit. *Appl. Phys. B* **122**, 254 (2016).
94. Le Cam, L. M. *Asymptotic methods in statistical decisiontheory* (Springer series in statistics Springer-Verlag, NewYork, 1986).
95. Hradil, Z. *et al. Phys. Rev. Lett.* **76**, 4295 (1996).
96. Pezze, L. Smerzi, A. Khoury, G. Hodelin, J F. & Bouwmeester, D. Phys. Rev. Lett. **99**, 223602 (2007).
97. Rubio, J. & Dunningham, J. *N. J. Phys.* **21**, 043037 (2019).
98. Olivares, S. & Paris, M. G. A. *J. Phys. B Atom. Mol. Opt. Phys.***42**, 055506 (2009).

99. Ishii, T., Kuwahara, T., Mori, T. & Hatano, N. Heating in integrable time-periodic systems. *Phys. Rev. Lett.* **120**, 220602 (2018).
100. Mishra, U., Prabhu, R. & Rakshit, D. Quantum correlations in periodically driven spin chains: Revivals and steady-state properties. *J. Magn. Magn. Mater.* **491**, 165546 (2019).
101. Mallayya, K. & Rigol, M. Heating rates in periodically driven strongly interacting quantum Many-Body systems. *Phys. Rev. Lett.* **123**, 240603 (2019).
102. Ye, B., Machado, F., White, C. D., Mong, R. S. K. & Yao, N. Y. Emergent hydrodynamics in nonequilibrium quantum systems. *Phys. Rev. Lett.* **125**, 030601 (2020).
103. Ji, K. & Fine, B. V. Suppression of heating in quantum spin clusters under periodic driving as a dynamic localization effect. *Phys. Rev. Lett.* **121**, 050602 (2018).
104. Rakcheev, A., & Läuchli, A.M. Estimating Heating Times in Periodically Driven Quantum Many-Body Systems via Avoided Crossing Spectroscopy. arXiv:2011.06017 (2018).

Acknowledgements

A.B. acknowledges support from the National Key R & D Program of China (Grant No.2018YFA0306703), the National Science Foundation of China (Grants No. 12050410253 and No. 92065115), and the Ministry of Science and Technology of China (Grant No. QNJ2021167001L). UM knowledges funding from the Chinese Postdoctoral Science Fund 2018M643437.

Author contributions

A.B. conceived the preliminary idea. U.M. obtained the data and produced the figures. U.M. and A.B. equally contributed to the analysis and writing of the manuscript.

Competing interests

The authors declare no competing interests.

Additional information

Supplementary Information The online version contains supplementary material available at https://doi.org/10.1038/s41598-022-17381-y.

Correspondence and requests for materials should be addressed to U.M. or A.B.

Reprints and permissions information is available at www.nature.com/reprints.

Publisher's note Springer Nature remains neutral with regard to jurisdictional claims in published maps and institutional affiliations.